Estimating permeability of partially frozen soil using floating random walks

Jiangzhi Chen[1,2], Shenghua Mei[1,2], Alan W. Rempel[3]

[1]Institute of Deep-Sea Science and Engineering, Chinese Academy of Sciences, Sanya, Hainan Province, 572000, China
[2]CAS Key Laboratory for Experimental Study under Deep-sea Extreme Conditions, Institute of Deep-sea Science and Engineering, Chinese Academy of Sciences, Sanya, Hainan Province, China
[3]Department of Earth Sciences, University of Oregon, Eugene, OR 97403, USA

Key Points:

- A floating random walk method is developed to estimate the effective permeability of porous media
- Effect of freezing on the permeability is approximated using terminated random walks
- Permeability of partially frozen soils is obtained using the soil freezing curves as input

Corresponding author: Jiangzhi Chen, `chenjz@idsse.ac.cn`

Abstract

Flow through partially frozen pores in granular media containing ice or gas hydrate plays an essential role in diverse phenomena including methane migration and frost heave. As freezing progresses, the frozen phase grows in the pore space and constricts flow paths so that the permeability decreases. Previous works have measured the relationship between permeability and volumetric fraction of the frozen phase, and various correlations have been proposed to predict permeability change in hydrology and the oil industry. However, predictions from different formulae can differ by orders of magnitude, causing great uncertainty in modeling results. We present a floating random walk method to approximate the porous flow field and estimate the effective permeability in isotropic granular media, without solving for the entire flow field in the pore space. In packed spherical particles, the method compares favorably with the Kozeny-Carman formula. We further extend this method with a probabilistic interpretation of the volumetric fraction of the frozen phase, simulate the effect of freezing in irregular pores, and predict the evolution of permeability. Our results can provide insight into the coupling between phase transitions and permeability change, which plays important roles in hydrate formation and dissociation, as well as in the thawing and freezing of permafrost and ice–bed coupling beneath glaciers.

1 Introduction

Fluid transport through porous granular media is important in understanding hydrate accumulation in marine sediments and frost heave in frozen soils. Take the hydrate-bearing sediment as an example: near the base of hydrate stability zone (BHSZ), methane-rich pore fluid migrates upward and affects the growth of hydrates in the pore space of marine sediments (Rempel, 2011; Cook & Malinverno, 2013; Wei et al., 2019; Liu et al., 2019). As the hydrate saturation S (i.e., pore volume fraction occupied by hydrate crystals) increases, hydrate crystals grow in the pore space, and the relative permeability k_r (i.e., the ratio of permeability of hydrate-bearing sediment to that of hydrate-free sediment) decreases. Moreover, when S approaches the percolation threshold, hydrate crystals grow beyond individual pores and form a connected mass (Tohidi et al., 2001), blocking most flow paths and leaving only very narrow liquid films so that k_r decreases dramatically. The low-permeability layer caused by hydrates seals further methane upwelling, which is crucial to creation of suitable hydrate storage and potential carbon sequestion strategies (e.g. Tohidi et al., 2010). A similar process occurs when ice lenses develop in frozen soils and cause frost heave (e.g. Nixon, 1991) and when frozen fringes form beneath glaciers and contribute towards enhanced bed strength (e.g. Meyer et al., 2018). In these cases the permeability reduction k_r caused by presence of the frozen phase (hydrate or ice) is a crucial control on the dynamics of solidification and melting.

Previous studies have measured the relation between k_r and either hydrate saturation (e.g., Liang et al., 2011; Kleinberg et al., 2003) or ice saturation (e.g., Chamberlain & Gow, 1979); empirical correlations based on these measurements are commonly employed in the oil industry (see Lee, 2008). However, predictions from different formulae can differ by orders of magnitude, bringing great uncertainty to modeling results. In response, some researchers have turned to computational fluid mechanics to solve for the flow field in the pore space, which can give more accurate results, but at high computation expense (e.g., Grenier et al., 2018). The sinuosity and interconnection of the pores space affects the transport process, and the nucleation of the frozen phase is intrinsically stochastic, both posing significant challenges to deterministic methods. Stochastic methods, on the contrary, focus on the disorderedness of the porous media, and consider the averaged fluid transport over the ensemble of individual pores and throats (e.g., Scheidegger, 1954; Schwartz & Banavar, 1989). Among these methods, the floating random walk method, also known as walk-on-spheres method, is widely used because it is easy to implement and capable of treating complex boundary conditions. The method was first proposed by Muller (1956) to solve Laplace equations, and was later extended to solve the Poisson equation (e.g., Haji-Sheikh & Sparrow, 1966; Delaurentis & Romero, 1990). The method does not require a regular lattice, and has been applied in studying groundwater diffusion problems (e.g., Lejay & Maire, 2013; Maire & Nguyen, 2016). Here, with the newly formed frozen phase approximated as randomly occurring boundaries, we extend the floating random walk method to account for the variations in pore structure that are caused by the blockages imposed by the frozen phase.

The paper is organized as follows: first, we briefly review the existing correlations used to predict the permeability of hydrate- or ice-bearing soils and sediments, and then we describe a floating random walk method to approximate the permeability in packed spherical particles, followed by a section extending the method to estimate the permeability evolution of granular media in which a frozen phase is present. For simplicity, the porous medium is assumed statistically isotropic, the external force is assumed homogeneous and time-independent, and gravity is neglected. We validate the method through comparison with experimental data extracted from the literature. Before concluding, we discuss briefly how the method might be improved further to better predict the effective permeability.

2 Existing permeability evolution models

Without the frozen phase, the permeability in saturated granular media is conveniently estimated using the Kozeny-Carman relation (Kozeny, 1927; Carman, 1937)

$$k_0 = \frac{\phi^3}{c(1-\phi)^2} D_{\text{eff}}^2 \tag{1}$$

where the constant c is typically taken as 180 (Kaviany, 1995), and the effective grain diameter D_{eff} can be calculated for a distribution of equant grains of size D_g using

$$D_{\text{eff}} = \frac{\sum D_g^3}{\sum D_g^2}. \tag{2}$$

After the onset of freezing, permeability reduction takes place with the relative permeability $k_r = k'/k_0$, a decreasing function of the frozen-phase saturation S. In Table 1 we summarize some widely used permeability models listed in Kleinberg et al. (2003, Appendix B) and Lee (2008, Appendix A). In semi-empirical treatments Archie's saturation exponent $1 < n < 2$ (Archie, 1942) is commonly used to account for the effects of differences in pore-scale location for the nucleated frozen phase. Of these models, the wall-coating model and center-occupying model are calculated using the lubrication approximation and hence are physically based, whereas the other models are semi-empirical or fully empirical. In Figure 1 these k_r predictions are plotted against the saturation S, using an Archie exponent $n = 1.5$. At moderate $S \approx 0.5$, their predictions can have discrepancies of up to three orders of magnitude.

Table 1. Existing permeability reduction models. The first two models are physically based, viewing the porous media as consisting of straight parallel capillary tubes with the frozen phase coating the walls or occupying the centers. Semi-empirical models use the Archie saturation exponent $1 < n < 2$ to account for the location of the frozen phase, and fully empirical models may have more parameters.

Type	Name	k_r
parallel capillaries	wall-coating	$(1-S)^2$
	center-occupying	$1 - S^2 + 2(1-S)^2/\ln S$
semi-empirical models	grain-coating [a]	$(1-S)^{n+1}$
	pore-filling [a]	$(1-S)^{n+2}/(1+\sqrt{S})^2$
empirical models	University of Tokyo [b]	$(1-S)^{M_S}$
	Lawrence Berkeley National Laboratory (LBNL) [c]	$\sqrt{S_w^*}\{1-[1-(S_w^*)^{1/m}]\}^2$, $S_w^* = (S_w - S_r)/(1-S_r)$

Parameters:
[a] $1 < n < 2$ is the Archie saturation exponent [b] $M_S = 10$ or 15 [c] $S_w = 1 - S$ is the volume fraction of water, $S_r = 0.9$ is the irreducible water saturation, and $m = 0.46$ is a fit parameter.

3 General theory

3.1 Flow in porous medium

A Newtonian fluid flowing at low Reynolds number through a porous medium must satisfy the conservation laws for mass and momentum. The mass conservation for single-phase incompressible steady flow requires

$$\boldsymbol{\nabla} \cdot \mathbf{u} = 0 \tag{3}$$

and the conservation of momentum without buoyancy and external forces gives

$$\mu \nabla^2 \mathbf{u} + \boldsymbol{\nabla} P = 0 \tag{4}$$

where P is the pressure, and μ is the viscosity of the fluid.

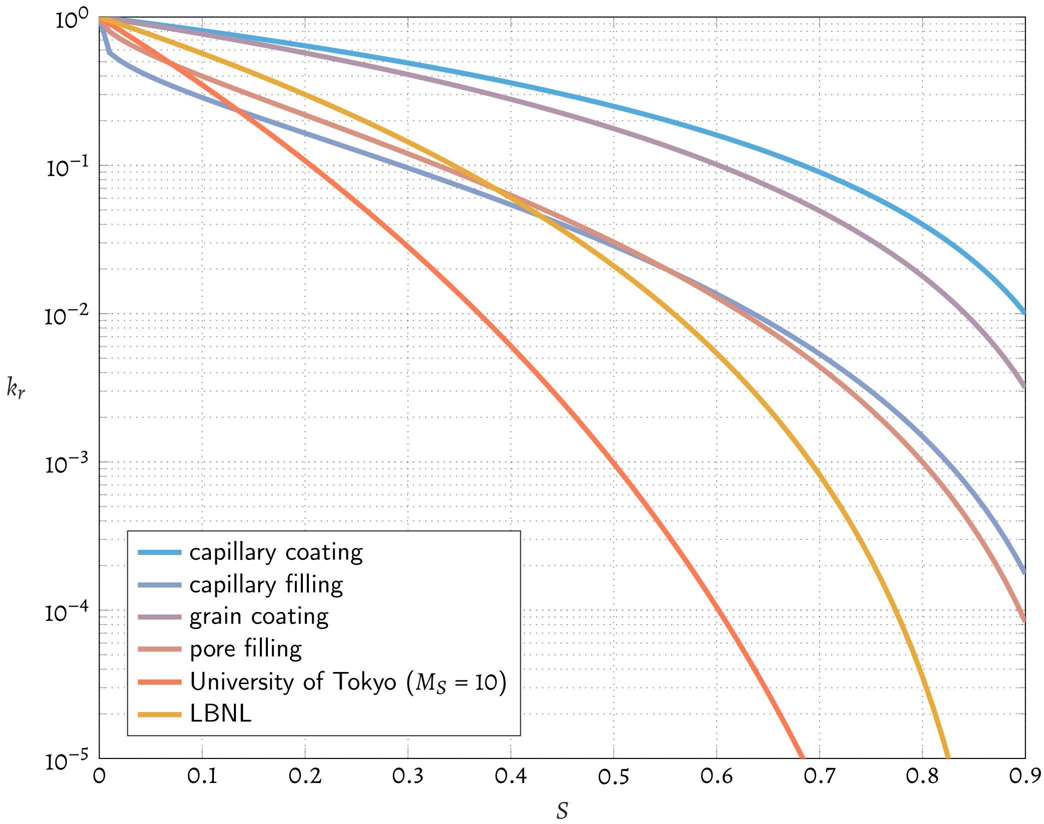

Figure 1. Existing models of permeability reduction with increasing hydrate or ice saturation. At moderate $S \approx 0.5$, the predictions may differ by up to three orders of magnitude.

Darcy's law states that the average fluid velocity $\mathbf{q} = \phi \langle \mathbf{u} \rangle$ is proportional to the pressure gradient across the fluid

$$\mathbf{q} = -\frac{\mathbf{k}}{\mu} \cdot \boldsymbol{\nabla} P \tag{5}$$

where $\mathbf{k}$ is the permeability tensor, determined by the microscopic structure of the medium. Note that the porosity ϕ is needed for the Darcy flux, which is an average over the entire cross-section. Combined with the mass conservation, the governing equation is

$$\boldsymbol{\nabla} \cdot (\mathbf{k} \boldsymbol{\nabla} P) = 0. \tag{6}$$

3.1.1 Poiseuille flow with constant pressure gradient

In a homogeneous medium, the permeability tensor is $\mathbf{k} = k\mathbf{I}$, and the pressure satisfies the Laplace equation $\nabla^2 P = 0$, with a solution of constant pressure gradient

$\mathbf{G} = \boldsymbol{\nabla} P$. The momentum conservation follows Poisson's equation for the flow field

$$\nabla^2 \mathbf{u} = -\frac{\mathbf{G}}{\mu}, \tag{7}$$

where both μ and $\mathbf{G}$ are treated as constant. Aligning the z-axis with $\mathbf{G}$, the resulting Poiseuille flow through an arbitrary cross-section $A \perp \mathbf{G}$ with boundary $\Gamma = \partial A$ is described by a velocity field $u(x, y)$ satisfying

$$\frac{\partial^2 u}{\partial x^2} + \frac{\partial^2 u}{\partial y^2} = -\frac{G}{\mu} \tag{8}$$

with a homogeneous no-slip boundary condition

$$u\Big|_{\Gamma} = 0. \tag{9}$$

The effective permeability is

$$k_{\text{eff}} = \frac{\phi \mu}{G} \langle u \rangle \tag{10}$$

where $\langle u \rangle$ is the spatially averaged fluid velocity.

3.1.2 Flow with varying pressure gradient

In disordered granular media, flow paths are constrained by the tortuous pore geometry. Hence, the pressure gradient varies spatially at the pore scale and deviations in its magnitude and direction from the macroscopic average must be evaluated numerically in deterministic treatments. However, the disorder of the porous medium implies that both the deviations in magnitude and direction of local gradients can be considered as randomly distributed. It is well established that k_{eff} can be approximated by the geometric mean of heterogeneously distributed local permeabilities $\hat{k}$ (see e.g., Matheron, 1967; Bakr et al., 1978; Gutjahr et al., 1978; Renard & de Marsily, 1997) in 2D isotropic media. Field measurements confirm that sampled $\hat{k}$ of relatively uniform soils follow a log-normal distribution (Law, 1944), and it is suitable to use the geometric mean of $\hat{k}$ as the effective permeability k_{eff} (Warren & Price, 1961). This greatly simplifies the problem, since the pressure gradient need not be evaluated explicitly throughout the pore space, and instead the effects of pore-scale variations in the pressure gradient can be treated statistically. An intuitive explanation of the log-normal distribution of sampled permeabilities is in Appendix A.

3.2 Floating random walk method

To find the averaged fluid velocity, we need to solve for the flow field at an arbitrary point $P_i = (x_i, y_i)$ in the 2D cross-section A of the pore space. We construct M random walks from P_i to the boundary Γ as follows (see Figure 2):

1. every random walk starts from $P_i^{(0)} = P_i$
2. in one walk, the walker is at a point $P_i^{(n)}$ after n steps
3. let ρ_n be the shortest distance between $P_i^{(n)}$ and Γ
4. a circle centered at $P_i^{(n)}$ with a radius ρ_n is constructed
5. a random point is chosen on the circle as the new location $P_i^{(n+1)}$
6. the walk is terminated when ρ_n is smaller than some prescribed small tolerance τ to the boundary.

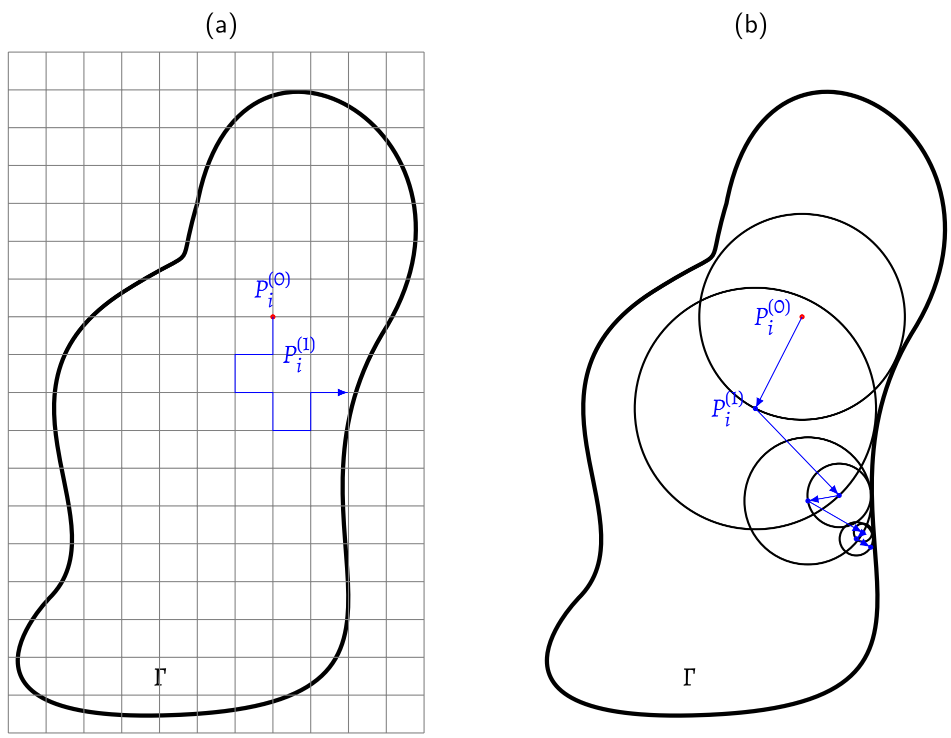

Figure 2. Schematics showing (a): fixed random walk in a domain with a grid. (b): floating random walk in the domain without a grid.

With a homogeneous boundary and constant G/μ, the value of u_i is

$$u_i \approx \frac{G}{4M\mu} \sum_{j=1}^{M} \sum_{n=1}^{K_j} \rho_n^2 \tag{11}$$

where K_j is the number of random steps required to reach the boundary in the j-th walk. The effective permeability becomes

$$k_{\text{eff}} \approx \frac{\phi}{4M} \left\langle \sum_{i=1}^{N} \sum_{j=1}^{M} \sum_{n=1}^{K_j} \rho_n^2 \right\rangle = \frac{2\phi}{M} \left\langle \sum_{j=1}^{M} \sum_{n=1}^{K_j} \hat{k}_n \right\rangle, \tag{12}$$

where $\hat{k}_n = \rho_n^2/8$ is the permeability of a hypothetical cylindrical tube of a radius ρ_n at the n-th step. The average number of steps in one walk is $K_j \sim \mathcal{O}(|\ln \tau|)$ (Delaurentis & Romero, 1990). Another way to interpret eq. (12) is that the effective permeability is a weighted mean of the permeabilities of the tubes. In implementing the algorithm, we choose $\tau/R_{\min} = 10^{-3}$ where R_m is the minimum radius of the particles comprising the porous medium. Errors arise from two sources: first, random walks introduce an error in estimating individual u_i, dependent on the value of τ; second, the averaging introduces an error related to the sample variance (Haji-Sheikh & Sparrow, 1966).

3.2.1 Floating random walk approach in straight ducts

In straight ducts, $\phi = 1$, and $\langle u \rangle$ can be approximated using the arithmetic mean of N points sampled uniformly within the boundary Γ of the duct

$$k_{\text{eff}} = \frac{\mu}{G} \langle u \rangle \approx \frac{\mu}{NG} \sum_{i=1}^{N} u_i \tag{13}$$

and $u_i = u(x_i, y_i)$ comes from solving Poisson's equation. It is easy to verify that floating random walk can calculate permeabilities of ducts of arbitrary cross-sections. Next we will apply the method on packed spherical particles.

3.2.2 Floating random walk on packed spherical particles

One major difference of granular media from straight ducts is that the local pressure gradient $\mathbf{G}_i'$ at the point (x_i, y_i) is different from the macroscopic pressure gradient $\mathbf{G}$. We still choose the cross-section $A \perp \mathbf{G}$, and the angle between the local gradient $\mathbf{G}_i'$ and $\mathbf{G}$ is $\psi_i < \pi/2$. In a small patch in the vicinity of (x_i, y_i), the local pressure gradient variation is negligible, and we can approximate u as satisfying

$$\nabla^2 u_i = -\frac{G_i'}{\mu} = -\frac{\chi_i G}{\mu} \tag{14}$$

where $\chi_i = G'_i/G$. The boundary condition of the small patch is still approximated as a homogeneous no-slip boundary, and the floating random walk leads to

$$u_i \approx \frac{\chi_i G}{4M\mu} \sum_{j=1}^{M} \sum_{n=1}^{K_j} \rho_n^2. \tag{15}$$

In the cross-section A, the component of the velocity through A is $u_i^\perp = u_i \cos\psi_i$, and the effective permeability is

$$k_{\text{eff}} \approx \frac{\phi\mu}{G} \left\langle u_i^\perp \right\rangle \approx \frac{\phi}{4M} \left\langle \chi_i \cos\psi_i \sum_{j=1}^{M} \sum_{n=1}^{K_j} \rho_n^2 \right\rangle = \frac{2\phi}{M} \left\langle \chi_i \cos\psi_i \sum_{j=1}^{M} \sum_{n=1}^{K_j} \hat{k}_n \right\rangle. \tag{16}$$

As argued in previous section, $\left\langle u_i^\perp \right\rangle$ is suitably approximated using the geometric mean instead of the arithmetic mean. A major simplification involves assuming $\psi \sim \mathcal{U}(0, \pi/2)$ rather than going through the process of evaluating the most appropriate angle from the exact pore geometry, because the packing is isotropic, these angles ought to be drawn from a uniform distribution. Also, we assume $\chi \sim \mathcal{U}(0, 1)$, and the distributions of ψ and χ are independent so that the geometric mean of random variables $\chi_i \cos\psi_i$ can be replaced with their expected value

$$k_{\text{eff}} \approx \frac{2\phi}{M} \left(\prod_{i=1}^{N} \chi_i \cos\psi_i \sum_{j=1}^{M} \sum_{n=1}^{K_j} \hat{k}_n \right)^{1/N} \approx \frac{\phi}{Me} \left(\prod_{i=1}^{N} \sum_{j=1}^{M} \sum_{n=1}^{K_j} \hat{k}_n \right)^{1/N}. \tag{17}$$

The detailed derivation of the simplification is given in Appendix B.

4 Permeability reduction due to emerging frozen phase

At the onset of its formation, the frozen phase (ice or hydrate) emerges in the pore space, blocks fluid flow paths, and reduces the permeability (Figure 3). As a simple demonstration, here we focus on the soil freezing case. The liquid saturation S_l is the volume fraction of pore liquid remaining in partially frozen pores, and the ice volume fraction $S = 1 - S_l$ can be treated as the probability of a random point within the pore space. Ice in the pores can terminate a random walk before the walker ever reaches the pore boundary Γ, thereby serving as an additional boundary. As a result, the expectation of ρ_n and the total number of steps K_j are reduced, and the effective porosity becomes ϕS_l, reducing the calculated permeability.

From Haji-Sheikh and Sparrow (1966), when choosing the next position of the walker $P^{(n+1)}$, instead of walking to a random position on a regular grid (Figure 2a), the floating random walk method moves the walker to a random position on a circle of a radius ρ_n

$$u(x_n, y_n) = \frac{1}{2\pi} \int_0^{2\pi} u(\rho_n, \omega) \mathrm{d}\omega = \int_0^1 u(\rho_n, \omega) \mathrm{d}F(\omega) \tag{18}$$

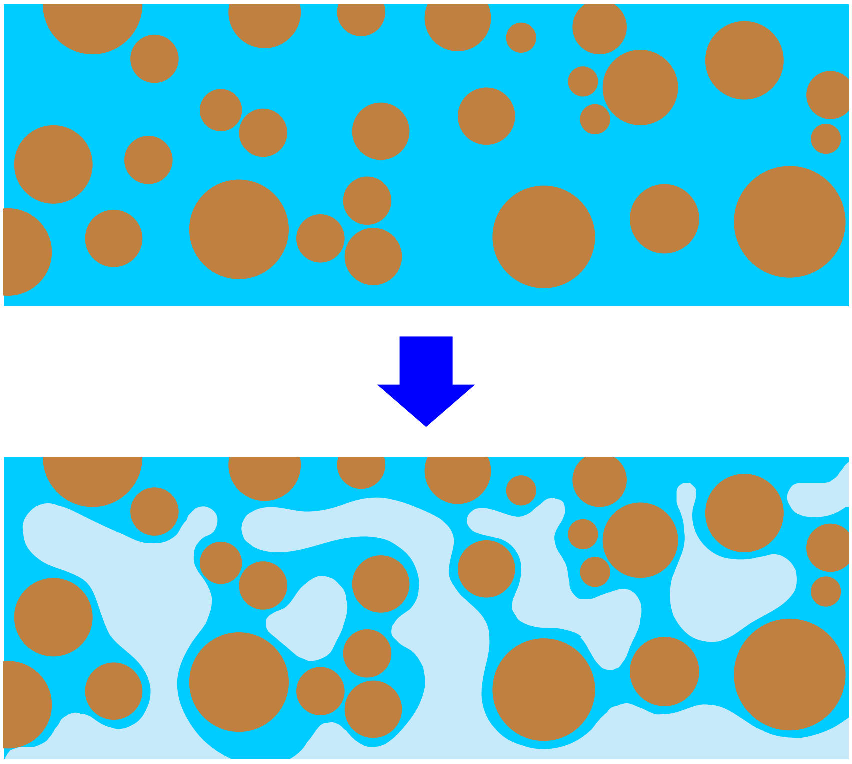

Figure 3. Schematic showing the frozen phase blocking the flow pathway. On the top brown circles are the solid particles saturated by water (blue). When ice or hydrate (white) grows in the pores, the flow paths are blocked, and the permeability is reduced.

where ω is the angular coordinate, $F = \omega/2\pi$ is the probability density and ρ_n is the radius of a circle centered at (x_n, y_n). In the original method, all walks are terminated at the boundary, or in other words, the boundary "absorbs" walkers. There is no radial contribution in F because there is no absorbing boundary within the circle, but when ice exists in the pore space, it can be treated as a new absorbing boundary, or "trap". Extensive research has been reported concerning random walks performed on regular lattices with known trap concentrations (e.g., Montroll & Scher, 1973) to study important properties including the survival probability of the walker after a large number of random steps. For a floating random walk without a lattice, however, it is difficult to estimate the survival probability of the walker because each step in the floating random walk is essentially a sum of numerous small segments of random walks in arbitrary directions, and in theory any point in the circle may be visited by the walker before it escapes the circle.

We take a novel approach to address this problem, which relies on terminated random walks. When the walker is at $P_i^{(n)}$ and the shortest distance from the walker to the particles is ρ_n, two random factors are involved in taking the next step in the pore space when ice may be present: first, the distribution of ice in the circle of radius ρ_n; and second, whether the direction of the walker's next step causes it to be absorbed by ice. We treat the ice distribution as unknown so that any point in the circle is equally likely to be frozen with a probability $p = S$. However, we anticipate that this assumption will introduce bias in the simulation, leading to further analysis in the discussion. Because the radial distribution function of uniform sampling in the circle of radius ρ_n is $\psi(r) = 2r/\rho_n^2$, eq. (18) in presence of additional randomly distributed absorbing boundaries is modified to

$$u(x_n, y_n) = \int_0^1 \mathrm{d}F(\omega) \int_0^{\rho_n} u(r, \omega)\psi(r)\mathrm{d}r. \tag{19}$$

The circle of radius ρ_n when no ice is present shrinks to a new circle of a radius $\sqrt{\xi}\rho_n$, where ξ is a random number drawn from $\mathcal{U}(0, 1)$. In every random step there is a probability p that the next position is on an icy absorbing boundary, and the walk is terminated. When there is no ice, i.e., $p = S = 0$, the original random walk scheme is recovered. Essentially, at $P^{(n)}$ we sample over all possible positions of $P^{(n+1)}$, and approximate the survival probability as a joint probability of subsequent successful steps.

4.1 Modified Kozeny-Carman formula

In addition to the stochastic method presented above, the Kozeny-Carman formula can also be extended to approximate the permeability in partially frozen soils with a simulated soil freezing curve relating the fraction of water remaining liquid in pore spaces to undercooling below bulk melting temperature. The porosity ϕ and effective diameter D_{eff} are changed with nucleated ice or hydrate crystals. Assuming that the new frozen phase occurs in the form of small spherical particles of the same size D_t, and the new effective diameter is

$$D'_{\text{eff}} = \frac{\sum D_g^3 + \sum D_t^3}{\sum D_g^2 + \sum D_t^2}. \tag{20}$$

The grain volume V_g and emerging frozen phase volume V_t are related using the remaining liquid fraction S_l,

$$\frac{\pi}{6} \sum D_g^3 = V_g = (1 - \phi)V \tag{21}$$

$$\frac{\pi}{6} \sum D_t^3 = V_t = (1 - S_l)\phi V \tag{22}$$

so

$$\sum D_t^3 = \frac{(1-S_l)\phi}{1-\phi} \sum D_g^3 \tag{23}$$

and combined with $\sum D_t^3 = D_t \sum D_t^2$, we have

$$\frac{D'_{\text{eff}}}{D_{\text{eff}}} = \frac{D_t(1-S_l\phi)}{D_t(1-\phi) + D_{\text{eff}}\phi(1-S_l)}. \tag{24}$$

Together with the reduced porosity $\phi' = S_l\phi$, we can predict the permeability reduction given D_t and S_l

$$k_r = \frac{S_l^3(1-\phi)^2}{(1-S_l\phi)^2} \frac{D'^2_{\text{eff}}}{D^2_{\text{eff}}}. \tag{25}$$

The emerging spherical particle size D_t can be estimated using the Gibbs-Thomson relation

$$D_t \approx \frac{4\gamma T_m}{\rho_i L \Delta T} \tag{26}$$

where the water-ice surface tension $\gamma \approx 0.029\,\text{J/m}^2$, ice density $\rho_i = 917\,\text{kg/m}^3$, ice latent heat $L = 3.34 \times 10^5\,\text{J/kg}$, and bulk melting point $T_m = 273.15\,\text{K}$. The liquid fraction S_l is related to the undercooling ΔT by the simulated soil freezing curve of Chen et al. (2020), where the soil particle size distribution is assumed to be log-normal $\ln\mathcal{N}(\mu, \sigma_d^2)$, and the synthetic soil models are generated using the algorithm from Kansal et al. (2002).

5 Validation and Results

5.1 Comparison with existing models

In Figure 4 we plot the floating random walk result for the mono-dispersed Finney pack (Finney, 1970) with other models listed in Table 1. For comparison, the modified Kozeny-Carman result is also shown as a black dashed curve. At low $S < 0.15$ our floating random walk result resembles the University of Tokyo result. For the entire range $S < 0.9$, our model is very close to the pore filling and capillary filling curves, consistent with the physical picture that the frozen phase is distributed in the pore space, especially at higher S. The modified Kozeny-Carman equation gives higher predictions for $S < 0.8$, but converges to the floating random walk model as S increases. At $S = 0.9$, our model result gives four orders of magnitude drop in k_r, similar to that of the modified Kozeny-Carman equation. The soil freezing curves are easy to calculate, and the modified Kozeny-Carman equation can be an adequate approximation for k_r.

It is worth noting that for synthetic soil models where the soil particle sizes $D \sim \ln\mathcal{N}(\mu, \sigma_d)$, if we keep the porosity ϕ unchanged, and let σ_d vary, for well-sorted particle

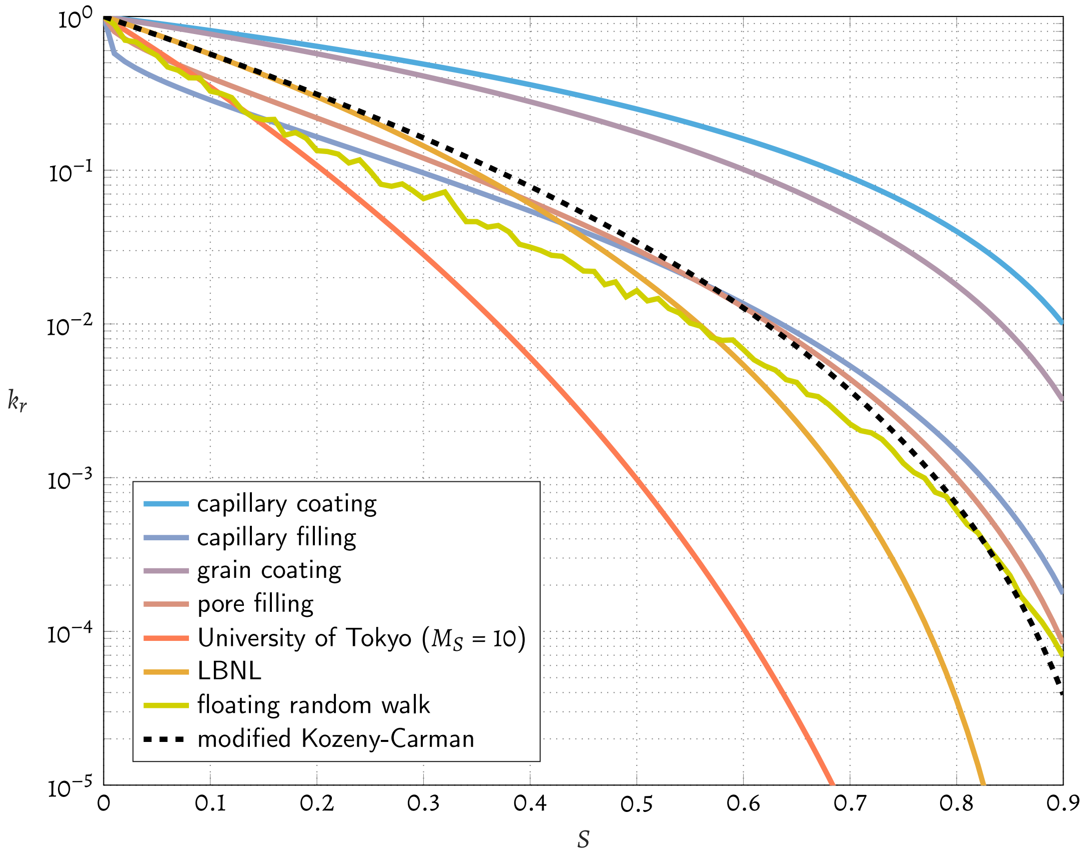

Figure 4. Simulated permeability reduction with increasing frozen phase saturation (yellow) using $N = 5000$ and $M = 200$, compared with existing permeability reduction models. At low $S < 0.15$, the floating random curve resembles the University of Tokyo model with $M_S = 10$, but its slope gradually becomes gentler. At higher S, the predicted k_r is close to the pore filling model. The modified Kozeny-Carman model is also shown as black dashed line for comparison.

sizes (i.e., small σ_d), the permeability reduction curves only change slightly. This suggests that certain properties of the pore space are invariant for synthetic soil models with well-sorted particle sizes.

5.2 Comparison with experimental data

The variation of permeability k with the ice or hydrate saturation is technically difficult to measure directly, and only a few reliable data sets have been published, using the hydraulic conductivity k_H instead of the permeability. With constant pressure head, the hydraulic conductivity is related to the permeability as

$$k_H = \frac{k\rho g}{\mu} \tag{27}$$

where the viscosity of water can be calculated using the empirical relation (Straus & Schubert, 1977)

$$\mu(T) = \mu_0 \exp\left(\frac{A}{T - B}\right) \tag{28}$$

where $\mu_0 = 2.414 \times 10^{-5}\,\mathrm{Pa\,s}$, $A = 570.58\,\mathrm{K}$ and $B = 140\,\mathrm{K}$. At $0\,°\mathrm{C}$, $\mu = 0.0018\,\mathrm{Pa\,s}$.

Watanabe and Osada (2016) reported the hydraulic conductivity in samples of Iwate andisol, Fujinomori silt loam and Tottori dune sand as a function of liquid water content under both frozen and unfrozen conditions, and the Fujinomori silt loam and Tottori dune sand parameters were reported previously in Watanabe and Wake (2009). Among the three soil samples, the Tottori dune sand has a mean particle diameter $d_m = 0.35\,\mathrm{mm}$ and a uniformity coefficient of 1.7, which is categorized as well sorted, corresponding to $\sigma_d \approx 0.34$ when fitted to a log-normal distribution. Figure 5 shows the simulated reduction of hydraulic conductivity with an ice-free $k_H^* = 1.6 \times 10^{-5}\,\mathrm{m/s}$, shown as a red line, together with the modified Kozeny-Carman result using the same k_H^*. Apparently, the measured data for $S < 0.75$ and $S > 0.75$ show different trends, possibly due to the coarse sand particle size. Our model fits nicely with the experimental data for $S > 0.75$.

There are other reports in the literature on the change of k_H against the undercooling below bulk melting temperature (e.g., Nixon, 1991, and references therein) with finer soils, which can be used for validation combined with the soil freezing curves. Horiguchi and Miller (1983) measured conductivities of six different sediments at subzero temperature as low as $-1\,°\mathrm{C}$, and we use the Manchester silt data because it has detailed grain size analysis, enabling the construction of a synthetic particle pack with realistic characteristics. The $4\,\mu\mathrm{m}$ to $8\,\mu\mathrm{m}$ fraction of Manchester silt is well sorted, and is approximated using mono-dispersed soil of a diameter of $6\,\mu\mathrm{m}$. Figure 6 compares the calculated conductivity evolution with undercooling, using calculated soil-freezing curves following Chen et al. (2020) and the ice-free $k_H^* = 2.6 \times 10^{-8}\,\mathrm{m/s}$. It is clear that the measurements, both the whole Manchester silt and the more well-sorted $4\,\mu\mathrm{m}$ to $8\,\mu\mathrm{m}$ fraction, generally follow the trend of the floating random walk simulation, but the well-sorted fraction fits the model better, and the whole Manchester silt data deviate more significantly as the pore space becomes increasingly filled by ice.

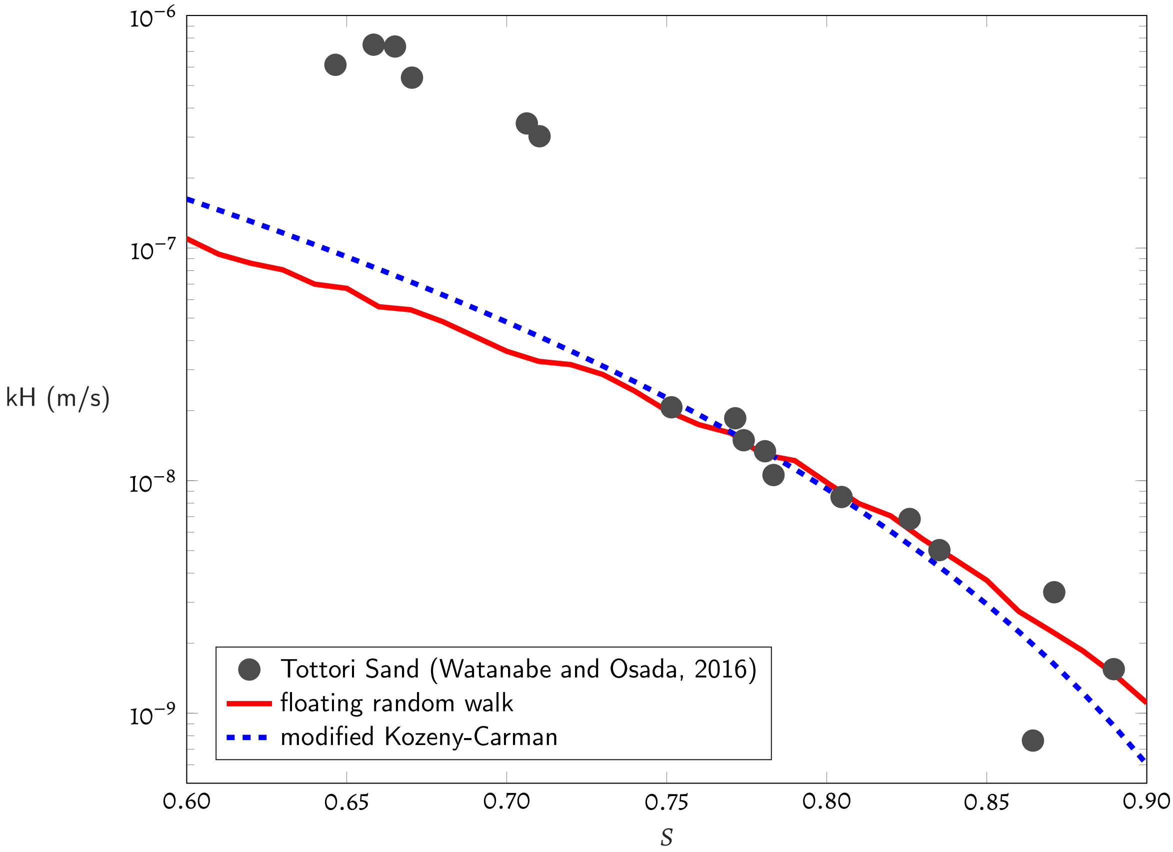

Figure 5. Simulated conductivity evolution of Tottori sand with ice saturation S. The solid dots are measurements from (Watanabe & Osada, 2016), and the red line is the simulated conductivity with an ice-free $k_H^* = 1.6 \times 10^{-5}$ m/s using $N = 5000$ and $M = 200$. The modified Kozeny-Carman result is shown in blue dashed line for comparison.

In both the Tottori sand and Manchester silt simulation, no adjustable parameters are needed to obtain the predictions, and we only need the ice-free conductivity and grain size distribution.

6 Discussion

6.1 Synthetic soil models

It is difficult to use a single functional relationship to describe the dependence of permeability on undercooling because changes in ice (or hydrate) saturation with undercooling, as well as its heterogeneous distribution, differ greatly between real sediments. Previous analytical models are commonly based on highly idealized geometries consisting of parallel

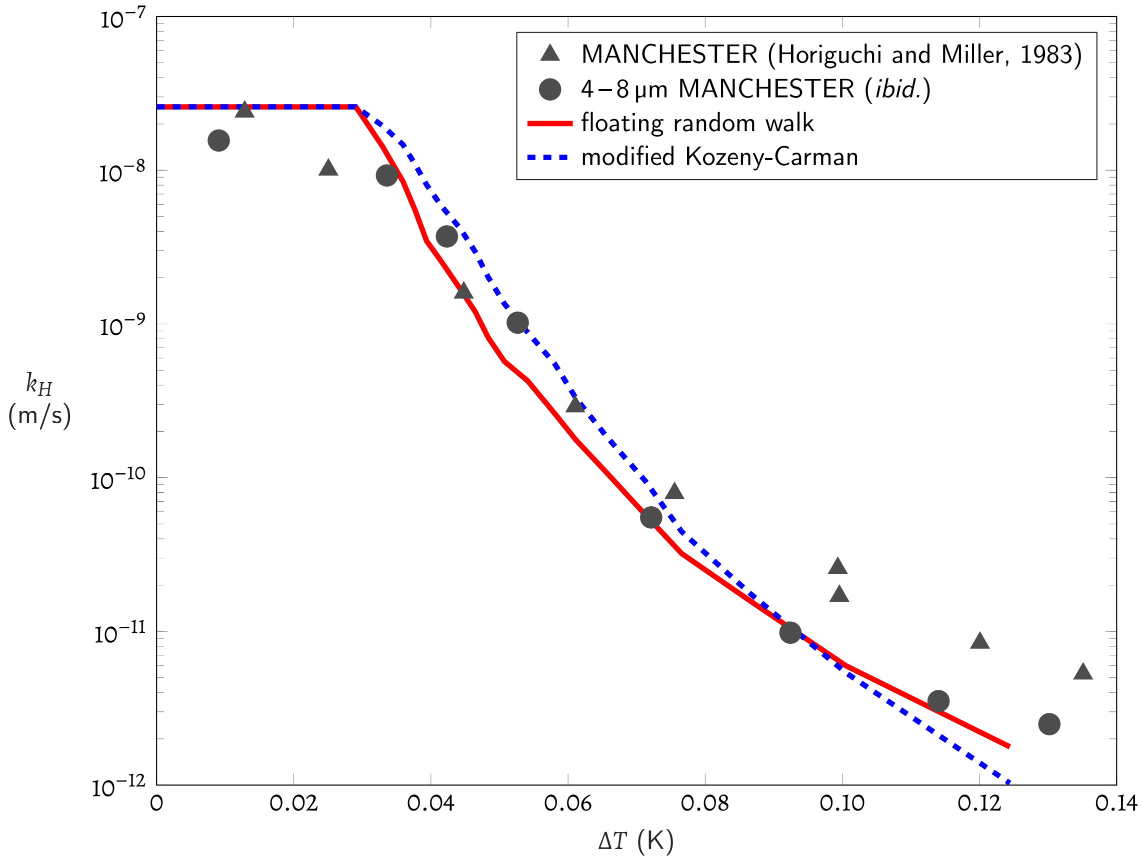

Figure 6. Hydraulic conductivity of Manchester silt decreases with undercooling below bulk freezing temperature. The black triangles are measurements of the Manchester silt, and the solid circles are the 4 µm to 8 µm fraction. The ice-free conductivity is chosen as $k_H^* = 2.6 \times 10^{-8}$ m/s. The permeability reduction simulated using the floating random walk with $N = 5000$ and $M = 200$ and the soil freezing curve is shown as red curve, and the blue dashed line is the modified Kozeny-Carman result. The deviation between the floating random walk curve and whole Manchester silt data increases at larger ΔT.

capillaries, or use the Archie saturation exponent to parameterize the contribution of tortuosity between packed grains. Other works assume that the pore space is fractal (e.g., Yu & Cheng, 2002). In our model we use synthetic model soils of packed grains, more closely mimicking real soils and sediments, while idealizing the grains as spherical to maintain tractability. Due to the limitations of packing algorithms, our approach is best suited for modeling relatively well-sorted soils and sediments, with the variance σ_d in the log-normal distribution less than 0.5, equivalent to about 0.72 in terms of the inclusive graphic standard deviation (Folk & Ward, 1957). In poorly-sorted soils, such as the Fujimori silt loam investigated by (Watanabe & Osada, 2016), smaller particles may fill in interstitial spaces between larger grains, and crucial parameters such as the porosity can vary significantly, making it difficult to sample potential flow paths adequately.

6.2 Biased distribution of absorbing ice boundary

When ice grows in the pores, we assume that ice is uniformly distributed in the pore space so that the absorbing boundary randomly occurs and changes the random walking steps, and we determine the next position of the walker by a point process. This is equivalent to treating the newly formed ice as a set of discrete points. However, in reality the emerging ice particles are spatially correlated, occupying the center of the pore space. Although we can find the interface curvature of ice particles using the Gibbs-Thomson equation, their geometry are constrained by the irregular pore walls, and their contributions to the walker survival probability are difficult to estimate without their locations. Extensions to this work that are directed towards approximating changes in pore-scale frozen phase distributions with undercooling hold promise for further improving relative permeability predictions.

6.3 Anticipated range of validity

At low saturation, ice (or hydrate) first occupies only the largest pores, invading smaller and smaller pores as the undercooling increases, with small residual liquid volumes remaining in premelted films that coat sediment particles and in liquid-filled crevices near particle contacts (e.g. Cahn et al., 1992; Chen et al., 2020). In the floating random walk we essentially approximate potential liquid flow paths with a weighted geometric mean of tubes, effectively neglecting the liquid crevices and films between ice and grains. However, as the ice or hydrate saturation grows, at some point most liquid water will remain in small reservoirs between the grains instead of in the pore centers. In mono-dispersed packing, we can estimate the critical liquid saturation below which the crevices dominate the flow paths using an averaging method inside a hypothetical triclinic cell formed by eight spherical grains, with each side being $2R$ and three angles α, β and γ (Bordia, 1984). Theoretically crevices can occur between particles not in contact, but as the distance between the two particles increases, it is much more difficult for liquid connecting the particles to form a concave meniscus with positive mean curvature. So in low liquid saturation conditions, most liquid stays in crevices between contacting particles (Figure 7), while at lower saturations still, the small volumes of liquid in premelted films coating ice–particle contacts are expected to dominate (e.g. Cahn et al., 1992; Chen et al., 2020).

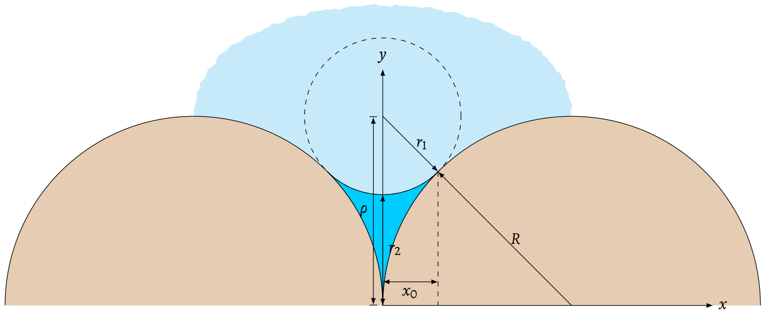

Figure 7. Crevice between two contacting mono-dispersed particles and ice. The ice grows in the pore (light blue), leaving only a small crevice for residual liquid (blue) which revolves around the x-axis. The dashed circle is the poloidal circle in the toroidal approximation.

As shown in Figure 7, the interface of liquid in the crevice is approximated using a torus, with the poloidal radius given by the inverse throat curvature r_1. The toroidal radius is ρ, and $r_2 = \rho - r_1$ is the second principal radius. Between contacting mono-dispersed particles of radius R, the crevice has volume

$$\begin{aligned} V =& 2\pi\left[(\rho^2 + r_1^2)x_0 - Rx_0^2 - \rho x_0\sqrt{r_1^2 - x_0^2} - r_1^2\rho\arctan\frac{R}{\rho}\right] \\ =& 2\pi r_1^2\left[R - \sqrt{r_1(r_1 + 2R)}\arctan\frac{R}{\rho}\right] \end{aligned} \tag{29}$$

which, keeping only the leading order, can be approximated to (Cahn et al., 1992)

$$V_c \sim 2\pi R r_1^2 \tag{30}$$

and in the triclinic cell there are three crevices, so the liquid saturation is

$$S_l = \frac{3V_c}{V_0} \approx \frac{6\pi R}{V_0} r_1^2. \tag{31}$$

The total pore volume V_0 is the volume of the triclinic cell minus the volume of a sphere, which is

$$V_0 = 8R^3\sqrt{1 - \cos^2\alpha - \cos^2\beta - \cos^2\gamma + 2\cos\alpha\cos\beta\cos\gamma} - \frac{4}{3}\pi R^3 \tag{32}$$

and the crevice volume is independent of α, β and γ. So the average liquid saturation is

$$\langle S_l\rangle = \left\langle\frac{3V_c}{V_0}\right\rangle = 3V_c\left\langle\frac{1}{V_0}\right\rangle = 3V_c\left(\frac{6}{\pi}\right)^3\int_{\frac{\pi}{3}}^{\frac{\pi}{2}}\int_{\frac{\pi}{3}}^{\frac{\pi}{2}}\int_{\frac{\pi}{3}}^{\frac{\pi}{2}}\frac{\mathrm{d}\alpha\,\mathrm{d}\beta\,\mathrm{d}\gamma}{V_0(\alpha,\beta,\gamma)} \approx \frac{1.089V_c}{R^3} \tag{33}$$

and with the expression for V_c, we can calculate the $\langle S_l \rangle$ curve for the low-saturation regime, mainly between $0.01 < S_l < 0.1$. The minimum possible pore radius inscribed between three mutually touching grains is $r^* = (2/\sqrt{3}-1)R$, and the crevice contributions become significant for $r_1 \leq r^*$, which gives the corresponding saturation $\langle S_l^* \rangle \approx 0.065$. Therefore, for ice saturation $S < 1-\langle S_l^* \rangle \approx 0.935$, the contributions of crevices (and liquid films) to the flow paths is expected to be insignificant and our floating random walk procedure should be most effective at capturing the dominant controls on relative permeability. For poly-dispersed grains, we cannot use the method above to properly estimate the range of validity, but since the permeability reduction curves change only slightly for well-sorted particles, the range of validity should be similar to the mono-dispersed case.

7 Conclusion

We demonstrate that the floating random walk method can conveniently predict the permeability of porous granular media, with a statistically simple, yet accurate, treatment of spatially varying pressure gradients. The method can be further extended to account for the emerging frozen phase, and estimate the permeability reduction caused by growing ice or gas hydrate in pores. The model predicts a permeability reduction similar to the pore filling model for moderate ice (or hydrate) saturation $S < 0.5$, and the reduction is smaller for higher $S > 0.5$. Combined with simulated soil freezing curves, our model results fit well with previously published measurements, with no adjustable parameters. Our approach provides a method to quantitatively estimate the permeability change within partially frozen soils, helps to understand the effects of frozen phase on the tortuosity, and sheds light on other transport properties in partially frozen soils.

Appendix A Geometric mean of permeability sampling

We assume that the permeability of interest is uniform in the direction parallel to the macroscopic pressure gradient, and the permeability tensor is then reduced to a scalar function $k(\mathbf{r})$. The governing equation becomes

$$\nabla^2 P + \boldsymbol{\nabla} P \cdot \boldsymbol{\nabla} \ln k = 0. \tag{A1}$$

Again, we let the z-axis be aligned with the macroscopic pressure gradient $\mathbf{G}$, and we write the pressure as composed of a mean pressure and a perturbed pressure $P = Gz+$

$h(\mathbf{r})$

$$\nabla^2 h + \boldsymbol{\nabla} h \cdot \boldsymbol{\nabla} \ln k = 0. \tag{A2}$$

Let $k = k_0 \exp(\xi)$, we have

$$\nabla^2 h + \boldsymbol{\nabla} h \cdot \boldsymbol{\nabla} \xi = 0. \tag{A3}$$

From the perspective of force balance, pressure gradient $\boldsymbol{\nabla} h$ is balanced by viscous frictional forces from the medium, which are additive. The central limit theorem ensures that the collective result is that the perturbation h on a 2D surface follows a Gaussian distribution in stochastic medium no matter what the original distribution of the frictional forces is

$$h(\mathbf{r}) \sim h_0 \exp\left(-\frac{1}{2\sigma_h^2}|\mathbf{r} - \mathbf{r}_0|^2\right) \tag{A4}$$

where the correlation between two arbitrary orthogonal directions is zero and σ_h is the variance. Then we can find that ξ also follows a Gaussian distribution with the same variance σ_h, which ensures that the sampled permeabilities follow a log-normal distribution.

Appendix B Expectation of products of random variables

When evaluating the geometric mean, we have

$$k'_{\text{eff}} \approx \frac{\phi}{4M}\left(\prod_{i=1}^{N} \chi_i \cos\psi_i \sum_{j=1}^{M}\sum_{n=1}^{K_j} \rho_n^2\right)^{1/N} = \frac{\phi}{4M}\left(\prod_{i=1}^{N} \chi_i \cos\psi_i\right)^{1/N}\left(\prod_{i=1}^{N}\sum_{j=1}^{M}\sum_{n=1}^{K_j} \rho_n^2\right)^{1/N}. \tag{B1}$$

Because χ_i and $\cos\psi_i$ are independent random variables, the first part can be replaced by their expectations

$$\lim_{N\to\infty}\left(\prod_{i=1}^{N} \chi_i \cos\psi_i\right)^{1/N} = \exp\left(\lim_{N\to\infty} \frac{\sum \ln\chi_i + \sum \ln\cos\psi_i}{N}\right) \tag{B2}$$

$$= \exp\left(\int_0^1 \ln x \mathrm{d}x\right) \exp\left(\int_0^1 \ln\cos\frac{\pi x}{2}\mathrm{d}x\right) = \frac{1}{2e} \tag{B3}$$

where $e \approx 2.71828$. Therefore,

$$k_{\text{eff}} \approx \frac{\phi}{8Me}\left(\prod_{i=1}^{N}\sum_{j=1}^{M}\sum_{n=1}^{K_j} \rho_n^2\right)^{1/N}. \tag{B4}$$

Acknowledgments

J.C. and S.M. would like supported by Chinese Academy of Sciences (No. QYZDY-SSW-DQC029), and J.C. was also supported by the National Natural Science Foundation of China (Grant No. 41804085). A.W.R. received funding from NSF-2012468. The relevant scripts and

data can be found on https://gitlab.com/jzchenjz/permeability-reduction, opensourced under the MIT license.

References

Archie, G. E. (1942, December). The electrical resistivity log as an aid in determining some reservoir characteristics. *Trans. AIME*, *146*(01), 54–62. doi: 10.2118/942054-g

Bakr, A. A., Gelhar, L. W., Gutjahr, A. L., & MacMillan, J. R. (1978, April). Stochastic analysis of spatial variability in subsurface flows: 1. comparison of one- and three-dimensional flows. *Water Resour. Res.*, *14*(2), 263–271. doi: 10.1029/wr014i002p00263

Bordia, R. (1984, July). A theoretical analysis of random packing densities of mono-sized spheres in two and three dimensions. *Scr. Metall.*, *18*(7), 725–730. doi: 10.1016/0036-9748(84)90328-4

Cahn, J., Dash, J., & Fu, H. (1992, September). Theory of ice premelting in monosized powders. *J. Cryst. Growth*, *123*(1-2), 101–108. doi: 10.1016/0022-0248(92)90014-a

Carman, P. C. (1937, December). Fluid flow through granular beds. *Chem. Eng. Res. Des.*, *15*, 150–166. doi: 10.1016/s0263-8762(97)80003-2

Chamberlain, E. J., & Gow, A. J. (1979, April). Effect of freezing and thawing on the permeability and structure of soils. *Eng. Geol.*, *13*(1-4), 73–92. doi: 10.1016/0013-7952(79)90022-x

Chen, J., Mei, S., Irizarry, J. T., & Rempel, A. W. (2020, October). A monte carlo approach to approximating the effects of pore geometry on the phase behavior of soil freezing. *J. Adv. Model. Earth Syst.*, *12*(10). doi: 10.1029/2020ms002117

Cook, A. E., & Malinverno, A. (2013, February). Short migration of methane into a gas hydrate-bearing sand layer at walker ridge, gulf of mexico. *Geochem. Geophys. Geosyst.*, *14*(2), 283–291. doi: 10.1002/ggge.20040

Delaurentis, J. M., & Romero, L. A. (1990, September). A monte carlo method for poisson's equation. *J. Comput. Phys.*, *90*(1), 123–140. doi: 10.1016/0021-9991(90)90199-b

Finney, J. L. (1970, November). Random packings and the structure of simple liquids. i. the geometry of random close packing. *Proc. R. Soc. London, Ser. A*, *319*(1539), 479–493. doi: 10.1098/rspa.1970.0189

Folk, R. L., & Ward, W. C. (1957, mar). Brazos river bar [texas]: a study in the significance of grain size parameters. *J. Sediment. Res.*, *27*(1), 3–26. doi: 10.1306/74d70646-2b21-11d7-8648000102c1865d

Grenier, C., Anbergen, H., Bense, V., Chanzy, Q., Coon, E., Collier, N., . . . Voss, C. (2018, apr). Groundwater flow and heat transport for systems undergoing freeze-thaw: Intercomparison of numerical simulators for 2d test cases. *Adv. Water Res.*, *114*, 196–218. doi: 10.1016/j.advwatres.2018.02.001

Gutjahr, A. L., Gelhar, L. W., Bakr, A. A., & MacMillan, J. R. (1978, October). Stochastic analysis of spatial variability in subsurface flows: 2. evaluation and application. *Water Resour. Res.*, *14*(5), 953–959. doi: 10.1029/wr014i005p00953

Haji-Sheikh, A., & Sparrow, E. M. (1966, March). The floating random walk and its application to monte carlo solutions of heat equations. *SIAM J. Appl. Math.*, *14*(2), 370–389. doi: 10.1137/0114031

Horiguchi, K., & Miller, R. D. (1983). Hydraulic conductivity functions of frozen materials. In *Proceedings of 4th international permafrost conference* (pp. 504–508). Fairbanks.

Kansal, A. R., Torquato, S., & Stillinger, F. H. (2002, November). Computer generation of dense polydisperse sphere packings. *J. Chem. Phys.*, *117*(18), 8212–8218. doi: 10.1063/1.1511510

Kaviany, M. (1995). *Principles of heat transfer in porous media.* Springer New York. doi: 10.1007/978-1-4612-4254-3

Kleinberg, R. L., Flaum, C., Griffin, D. D., Brewer, P. G., Malby, G. E., Peltzer, E. T., & Yesinowski, J. P. (2003, October). Deep sea NMR: Methane hydrate growth habit in porous media and its relationship to hydraulic permeability, deposit accumulation, and submarine slope stability. *J. Geophys. Res. Solid Earth*, *108*(B10). doi: 10.1029/2003JB002389

Kozeny, J. (1927). Über kapillare leitung des wassers im boden. *Royal Academy of Science, Vienna, Proc. Class I*, *136*, 271–306.

Law, J. (1944, December). A statistical approach to the interstitial heterogeneity of sand reservoirs. *Trans. AIME*, *155*(01), 202–222. doi: 10.2118/944202-g

Lee, M. W. (2008). *Models for gas hydrate-bearing sediments inferred from hydraulic permeability and elastic velocities. scientific investigations report 2008-5219* (Tech. Rep.).

Lejay, A., & Maire, S. (2013, June). New monte carlo schemes for simulating diffusions in discontinuous media. *J. Comput. Appl. Math.*, *245*, 97–116. doi: 10.1016/j.cam.2012.12.013

Liang, H., Song, Y., Chen, Y., & Liu, Y. (2011, January). The measurement of permeability of porous media with methane hydrate. *Pet. Sci. Technol.*, *29*(1), 79–87. doi: 10.1080/10916460903096871

Liu, J., Haeckel, M., Rutqvist, J., Wang, S., & Yan, W. (2019, May). The mechanism of methane gas migration through the gas hydrate stability zone: Insights from numerical simulations. *J. Geophys. Res. Solid Earth*. doi: 10.1029/2019jb017417

Maire, S., & Nguyen, G. (2016, March). Stochastic finite differences for elliptic diffusion equations in stratified domains. *Math. Comput. Simulation*, *121*, 146–165. doi: 10.1016/j.matcom.2015.09.008

Matheron, G. (1967). *Eléments pour une théorie des milieux poreux* (Tech. Rep.). ((in French))

Meyer, C. R., Downey, A. S., & Rempel, A. W. (2018, August). Freeze-on limits bed strength beneath sliding glaciers. *Nat. Commun.*, *9*(1). doi: 10.1038/s41467-018-05716-1

Montroll, E. W., & Scher, H. (1973, oct). Random walks on lattices. IV. continuous-time walks and influence of absorbing boundaries. *J. Stat. Phys.*, *9*(2), 101–135. doi: 10.1007/bf01016843

Muller, M. E. (1956, September). Some continuous monte carlo methods for the dirichlet problem. *Ann. Math. Stat*, *27*(3), 569–589. doi: 10.1214/aoms/1177728169

Nixon, J. F. D. (1991, December). Discrete ice lens theory for frost heave in soils. *Can. Geotech. J.*, *28*(6), 843–859. doi: 10.1139/t91-102

Rempel, A. W. (2011, October). A model for the diffusive growth of hydrate saturation anomalies in layered sediments. *J. Geophys. Res. Solid Earth*, *116*(B10). doi: 10.1029/2011jb008484

Renard, P., & de Marsily, G. (1997, October). Calculating equivalent permeability: a review. *Adv. Water Res.*, *20*(5-6), 253–278. doi: 10.1016/s0309-1708(96)00050-4

Scheidegger, A. E. (1954, August). Statistical hydrodynamics in porous media. *J. Appl. Phys.*, *25*(8), 994–1001. doi: 10.1063/1.1721815

Schwartz, L. M., & Banavar, J. R. (1989, June). Transport properties of disordered continuum systems. *Phys. Rev. B*, *39*(16), 11965–11970. doi: 10.1103/physrevb.39.11965

Straus, J. M., & Schubert, G. (1977, January). Thermal convection of water in a porous medium: Effects of temperature- and pressure-dependent thermodynamic and transport properties. *J. Geophys. Res.*, *82*(2), 325–333. doi: 10.1029/jb082i002p00325

Tohidi, B., Anderson, R., Clennell, M. B., Burgass, R. W., & Biderkab, A. B. (2001, September). Visual observation of gas-hydrate formation and dissociation in synthetic porous media by means of glass micromodels. *Geology*, *29*(9), 867. doi: 10.1130/0091-7613(2001)029⟨0867:vooghf⟩2.0.co;2

Tohidi, B., Yang, J., Salehabadi, M., Anderson, R., & Chapoy, A. (2010, February). Co2 hydrates could provide secondary safety factor in subsurface sequestration of CO2. *Environ. Sci. Technol.*, *44*(4), 1509–1514. doi: 10.1021/es902450j

Warren, J. E., & Price, H. S. (1961, September). Flow in heterogeneous porous media. *Soc. Pet. Eng. J.*, *1*(03), 153–169. doi: 10.2118/1579-g

Watanabe, K., & Osada, Y. (2016, May). Comparison of hydraulic conductivity in frozen saturated and unfrozen unsaturated soils. *Vadose Zone Journal*, *15*(5), vzj2015.11.0154. doi: 10.2136/vzj2015.11.0154

Watanabe, K., & Wake, T. (2009, oct). Measurement of unfrozen water content and relative permittivity of frozen unsaturated soil using NMR and TDR. *Cold Reg. Sci. Technol.*, *59*(1), 34–41. doi: 10.1016/j.coldregions.2009.05.011

Wei, L., Cook, A., Daigle, H., Malinverno, A., Nole, M., & You, K. (2019, August). Factors controlling short-range methane migration of gas hydrate accumulations in thin coarse-grained layers. *Geochem. Geophys. Geosyst.*. doi: 10.1029/2019gc008405

Yu, B., & Cheng, P. (2002, July). A fractal permeability model for bi-dispersed porous media. *Int. J. Heat Mass Transfer*, *45*(14), 2983–2993. doi: 10.1016/s0017-9310(02)00014-5

Figure 1.

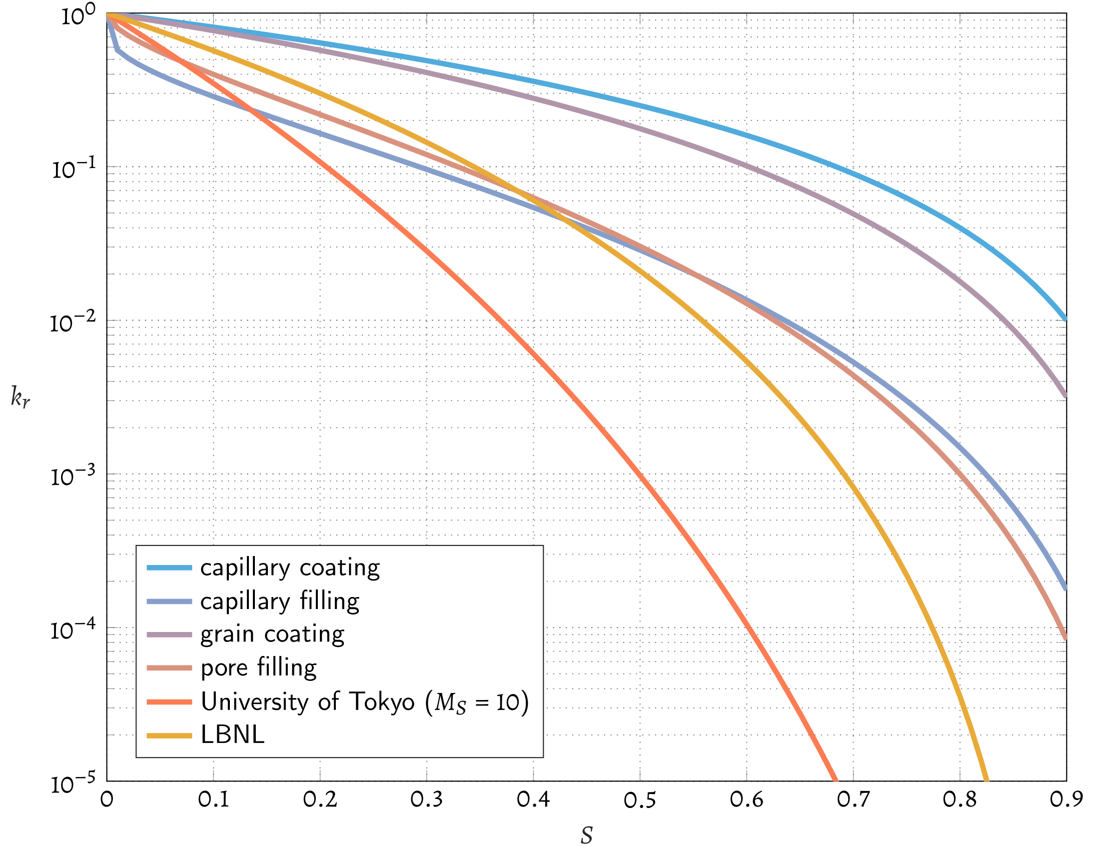

10^0
10^{-1}
10^{-2}
10^{-3}
10^{-4}
10^{-5}
k_r
0
0.1
0.2
0.3
0.4
0.5
0.6
0.7
0.8
0.9
S
capillary coating
capillary filling
grain coating
pore filling
University of Tokyo ($M_S = 10$)
LBNL

Figure 2.

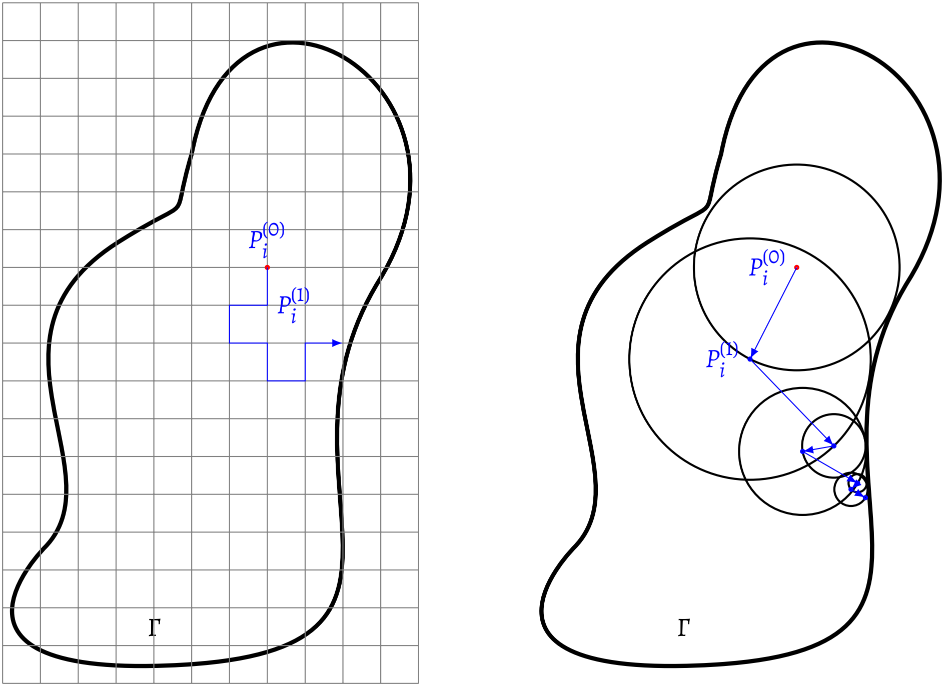
$P_i^{(0)}$
$P_i^{(1)}$
Γ
$P_i^{(0)}$
$P_i^{(1)}$
Γ

Figure 3.

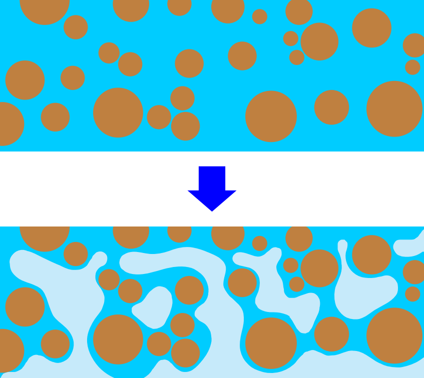

Figure 4.

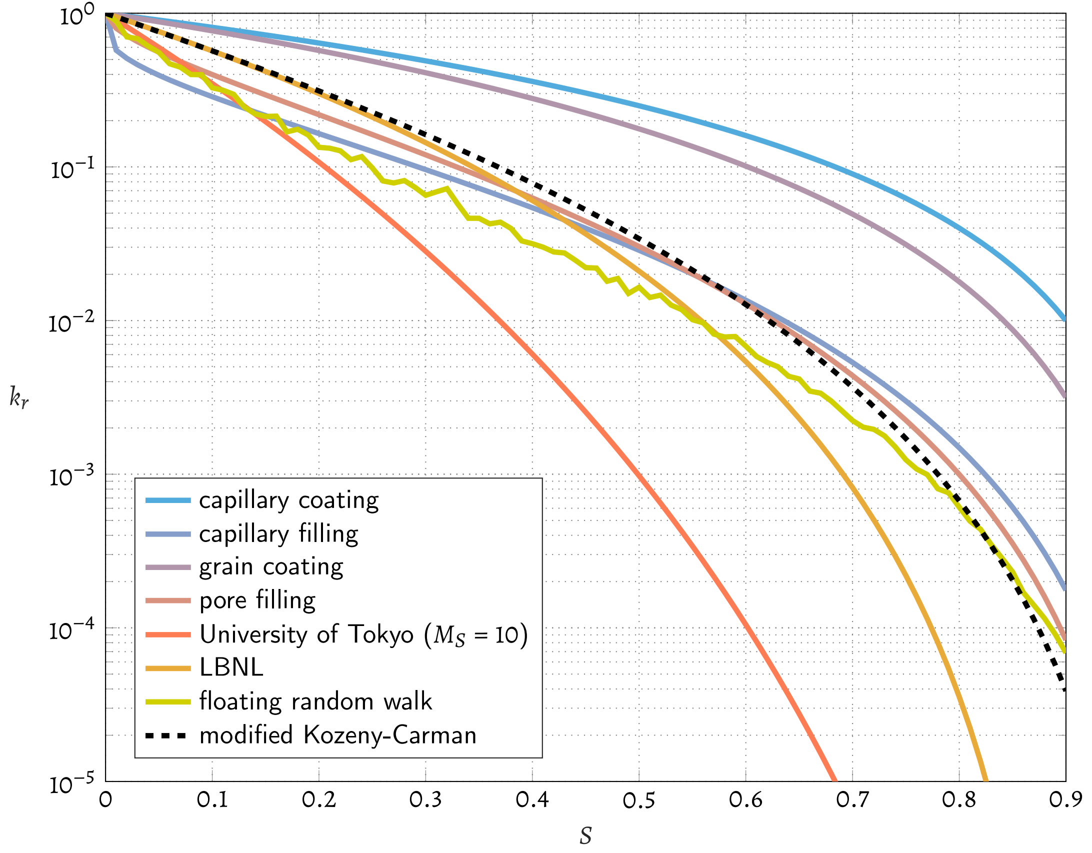

10^{0}
10^{-1}
10^{-2}
10^{-3}
10^{-4}
10^{-5}
k_r
0
0.1
0.2
0.3
0.4
0.5
0.6
0.7
0.8
0.9
S
capillary coating
capillary filling
grain coating
pore filling
University of Tokyo ($M_S = 10$)
LBNL
floating random walk
modified Kozeny-Carman

Figure 5.

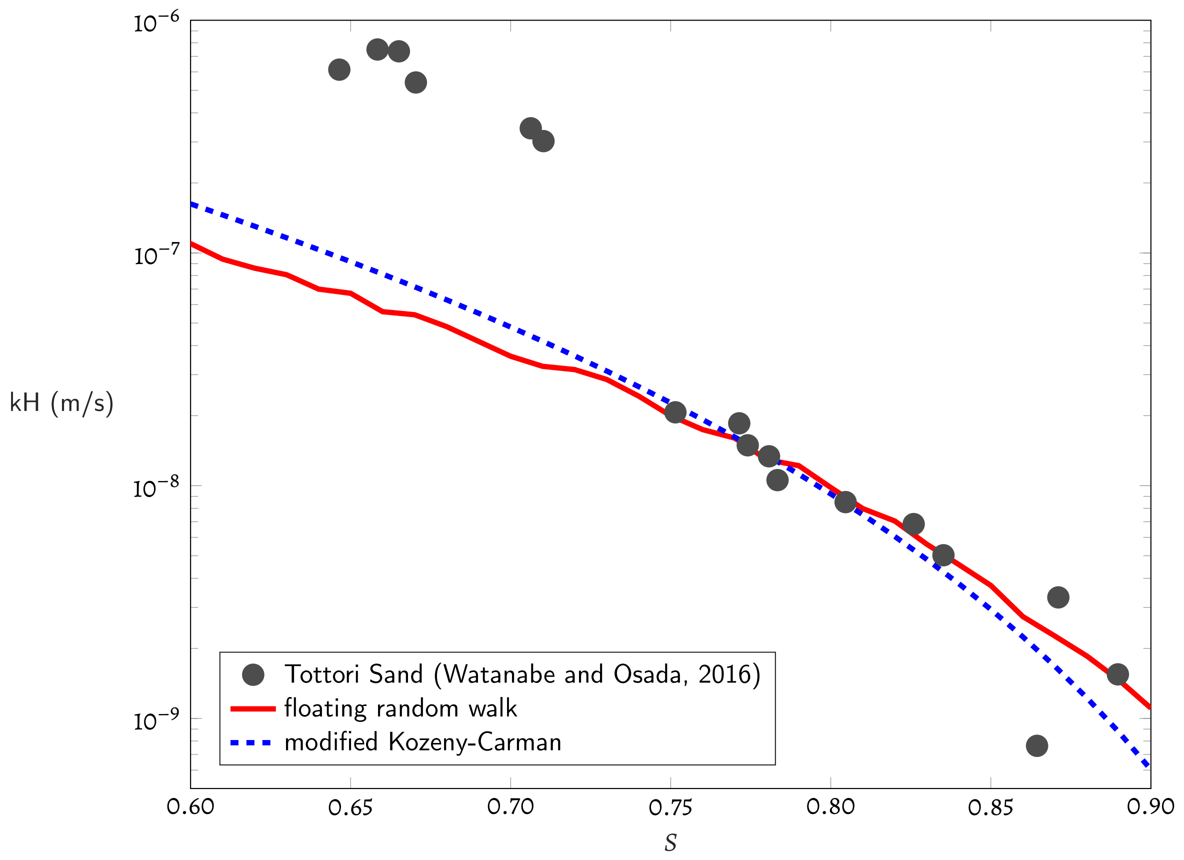

10^{-6}
10^{-7}
10^{-8}
10^{-9}
kH (m/s)
0.60
0.65
0.70
0.75
0.80
0.85
0.90
S
Tottori Sand (Watanabe and Osada, 2016)
floating random walk
modified Kozeny-Carman

Figure 6.

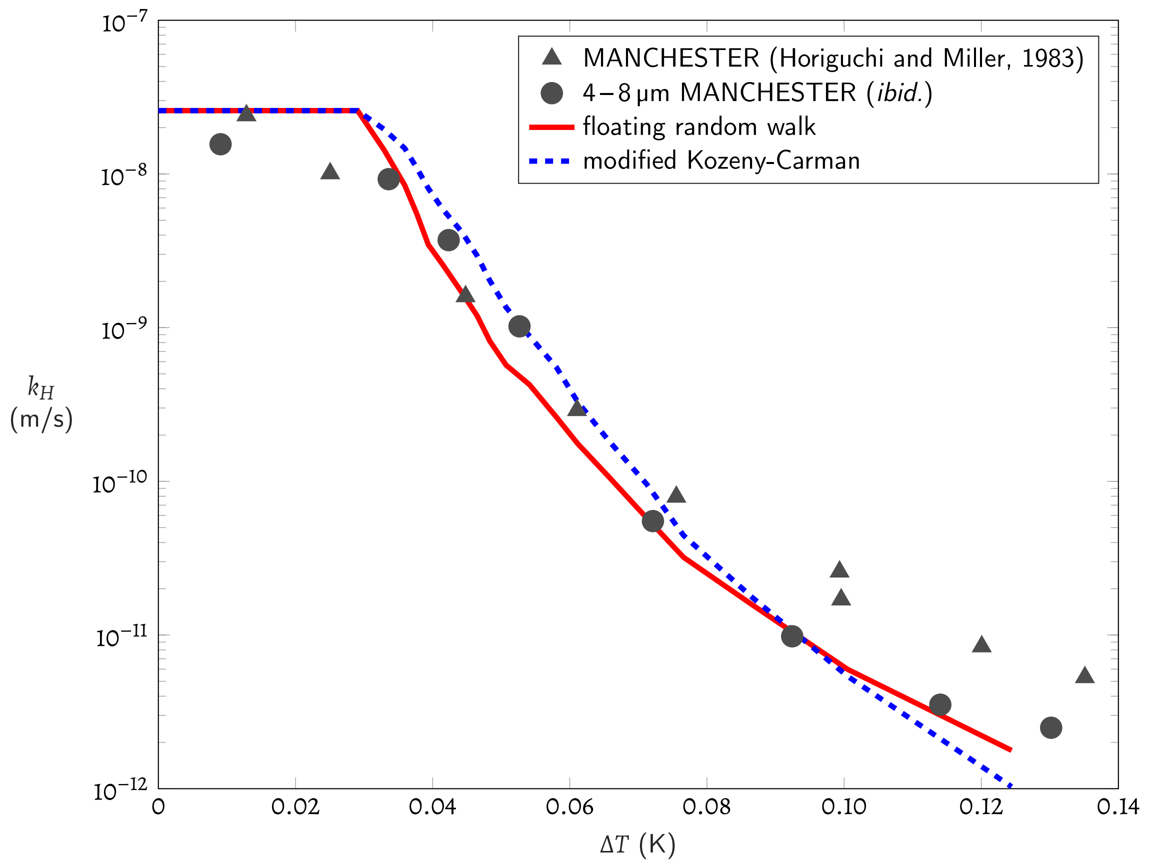

MANCHESTER (Horiguchi and Miller, 1983)
4−8 μm MANCHESTER (ibid.)
floating random walk
modified Kozeny-Carman
k_H (m/s)
10^{-7}
10^{-8}
10^{-9}
10^{-10}
10^{-11}
10^{-12}
0
0.02
0.04
0.06
0.08
0.10
0.12
0.14
ΔT (K)

Figure 7.

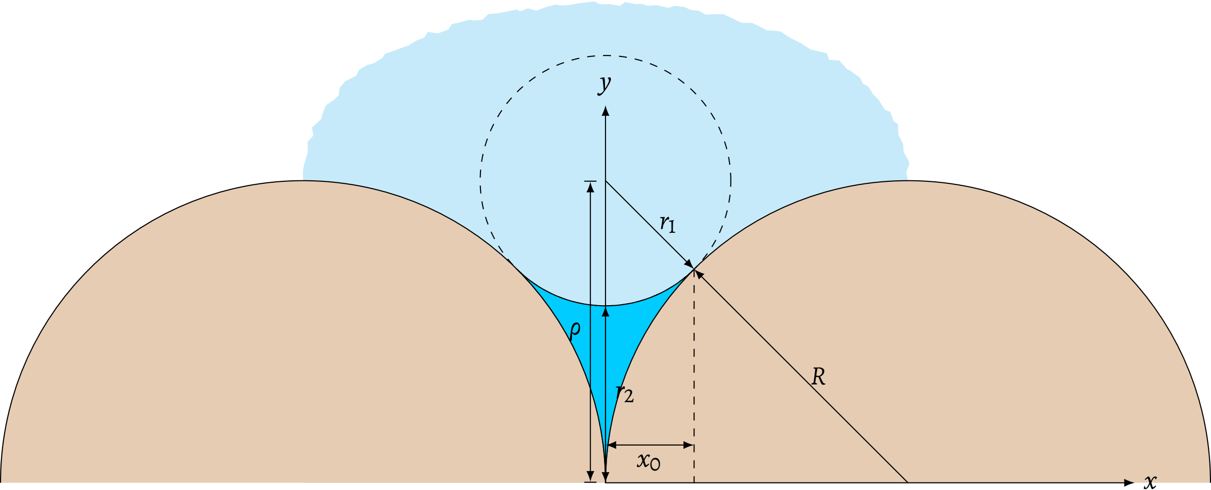

y
r1
ρ
r2
R
x0
x